Enhanced thermoelectric properties of heavy-fermion compounds Yb$_x$Ce$_y$Sm$_z$Ir$_2$Zn$_{20}$ ($x + y + z = 1$)

Jorge R. Galeano-Cabral [1,2] Eliana Karr,[2] Benny Schundelmier,[2,3] Olatunde Oladehin,[2,3] Eun S. Choi,[2,3]
Theo Siegrist,[2,4] Juan Ordonez,[1] Sarvjit Shastri,[5] Valeri Petkov,[6] Ryan E. Baumbach,[2,3] and Kaya Wei [2,*]

[1]*Department of Mechanical Engineering, FAMU-FSU College of Engineering, Tallahassee, Florida 32310, USA*
[2]*National High Magnetic Field Laboratory, Florida State University, Tallahassee, Florida 32310, USA*
[3]*Department of Physics, Florida State University, Tallahassee, Florida 32306, USA*
[4]*Department of Chemical and Biomedical Engineering, FAMU-FSU College of Engineering, Tallahassee, Florida 32310, USA*
[5]*X-ray Science Division, Argonne National Laboratory, Argonne, Illinois 60439, USA*
[6]*Department of Physics, Central Michigan University, Mount Pleasant, Michigan 48859, USA*

Thermoelectric materials hold tremendous promise for advances in fundamental science and practical applications, particularly for robust electricity generation in extreme and remote environments. Despite this, for most materials the energy conversion efficiency is limited by the proportionality between the electrical and thermal conductivities and small values of the Seebeck coefficient for metals. It was previously reported that the heavy-fermion compound YbIr$_2$Zn$_{20}$ exhibits large Seebeck coefficient [E. Mun *et al.*, Phys. Rev. B **86**, 115110 (2012)] and thermoelectric figure of merit ZT at 35 K [K. Wei *et al.*, Sci. Adv. **5**, eaaw6183 (2019)]. This behavior is primarily associated with strong hybridization between the f- and conduction electron states. Here, we seek to improve the thermoelectric properties through chemical substitution on the Yb site using Ce and Sm. By surveying different levels of substitution, we find that the thermoelectric properties vary strongly with the f-element ratio. This confirms that electronic hybridization dominates the thermoelectric properties and clarifies directions for optimizing these materials for applications. We also investigate the impact of the disorder on the thermal conductivity, where we find only weak variation with lanthanide content.

I. INTRODUCTION

During the past several decades it has been recognized that refrigerant fluids have substantial environmental impacts [1], even as the demand for cooling operations (e.g., for electronics) has increased [2]. A possible solution is found in thermoelectric materials, where electrical voltages are transformed into temperature gradients (and vice versa), but most such materials do not exhibit high efficiencies for power conversion. This is due to the intrinsic limitations of standard metals and semiconductors, where the electrical (σ) and thermal (κ) conductivities are proportional to each other [3]. A strategy to overcome this is offered by the "phonon-glass electron-crystal" concept presented by Slack [4]. Here, the crystal structure is optimized to suppress the lattice component of the thermal conductivity (κ_L), while the electronic properties are tuned to promote the electrical conduction and conversion of temperature gradients to electrical voltage [5–7]. Among such materials, it is especially useful to find examples that also exhibit enhanced Seebeck coefficients ($S = \Delta V/\Delta T$), where strongly correlated electron metals are promising candidates [8–10]. For these systems, the hybridization between the f- and conduction electron states results in Kondo-lattice hybridization, which renormalizes the Fermi surface such that there is a large and rapidly

changing density of states near the Fermi energy [11–13]. This distinctive behavior not only produces enhanced Seebeck coefficients, but also is highly tunable using chemical substitution, applied pressure, and magnetic fields [12]. Thus, there is a long-standing interest in cagelike structures with unconventional phonon scattering (e.g., filled skutterudites) that also host f-electron elements that encourage Kondo lattice formation (e.g., Ce, Yb, and U) [11,14–17].

The compounds YbT_2Zn$_{20}$ ($T =$ Co, Rh, Ir) have been investigated in this context because they feature cagelike structures with large unit cells and Kondo lattice physics [8,9,18]. They form in cubic structures with large lattice constants ($a = 14.165$ Å for $T =$ Ir) where the Yb ions are separated at a distance of 6.14 Å [19]. Measurements of their bulk thermodynamic and electrical transport properties reveal that the Yb ions adopt the 3+ valence state and that electronic hybridization produces mass enhanced charge carrier quasiparticles [9,14,19]. Among them, YbIr$_2$Zn$_{20}$ has attracted close interest owing to its metamagnetic behavior [18–20] and for having a large thermoelectric figure of merit ($ZT = S^2\sigma T/\kappa = 0.07$) at 35 K [9]. To our knowledge, this is only second to Bi$_{1-x}$Sb$_x$ at this temperature ($ZT = 0.15$) [21,22]. This motivated us to continue the investigations of this system by tuning the electronic state, the thermal conductivity, and the lattice anharmonicity through the substitution of Yb with Ce or Sm. While CeIr$_2$Zn$_{20}$ exhibits intermediate valence behavior [23], the behavior of SmIr$_2$Zn$_{20}$ is unknown but would be expected to resemble that of the weakly cor-

*Corresponding author: kwei@magnet.fsu.edu

TABLE I. Magnetization parameters from a Curie-Weiss fit, fitting parameters for C_p and C_p/T curves, relevant characteristic temperatures, and lattice parameters a of $Yb_xCe_ySm_zIr_2Zn_{20}$ ($x + y + z = 1$), where μ_{eff} and $\mu_{eff,Th}$ have units in μ_B, β has units in mJ mol^{-1} K^{-4}, a in Å, and all other variables shown in the table have units in degrees Kelvin.

Number	Composition	θ_W	μ_{eff}	$\mu_{eff,Th}$	β	θ_D	θ_E	T_{min}^S	T_{max}^ρ	a
1	$YbIr_2Zn_{20}$	−7.6	4.1	4.5	4.0	240	110	26.0	19.4	14.140
2	$Yb_{0.6}Ce_{0.4}Ir_2Zn_{20}$	−6.5	3.4	3.7	4.2	307.8	102.1	19.2	56.4	14.165
3	$Yb_{0.87}Ce_{0.08}Sm_{0.05}Ir_2Zn_{20}$	−32.4	4.0	4.2	3.7	291.6	97.1	19.8	50.2	14.162
4	$Yb_{0.77}Ce_{0.21}Sm_{0.02}Ir_2Zn_{20}$	−12.6	3.6	4.0	4.2	276.8	93.8	22.5	73.7	14.292
5	$Yb_{0.43}Ce_{0.13}Sm_{0.44}Ir_2Zn_{20}$	−16.7	2.7	2.7	3.5	302.7	102.4	18.7	68.9	14.274
6	$Yb_{0.33}Ce_{0.44}Sm_{0.23}Ir_2Zn_{20}$	−18.2	1.8	1.7	3.6	300.2	102.9	14.5	44.3	14.276

related antiferromagnet $SmRh_2Zn_{20}$ [24]. Also important is that while $YbIr_2Zn_{20}$ features a Fermi surface that is net electronlike [9], $CeIr_2Zn_{20}$ is likely to be net holelike [23]. Thus, it can be anticipated that Yb → Ce chemical substitution may simultaneously tune the charge carrier balance and the hybridization strength while Yb → Sm would dilute the Kondo lattice, weaken the hybridization, and introduce magnetic fluctuations. The ability to tune between n and p type opens up novel possibilities for these materials in terms of applications, finding the p-type counterparts for n-type $Bi_{1-x}Sb_x$, for instance. In addition, the introduction of multiple lanthanides with differing masses may suppress the phonon contribution to the thermal conductivity. Finally, the different size of Ce, Sm, and Yb allows us to explore the effects of local lattice strain and deformation of the underlying framework of Zn atoms. In this study we synthesized five different compositions of high-quality single crystals of $Yb_xCe_ySm_zIr_2Zn_{20}$ ($x + y + z = 1$), listed in Table I (Nos. 2–6).

In Sec. III A, we survey the electrical transport and thermoelectric properties in this series to establish the impact of f-block chemical substitution. In Sec. III B we examine the impact of chemical substitution on the magnetic properties, which provides insights into the f-electron valence and hybridization between the f- and conduction electron states. In Sec. III C we investigate the atomic structure using high-energy x-ray diffraction (XRD) coupled to an atomic pair distribution function (PDF) analysis. These measurements collectively clarify the parameters that control the behavior of $YbIr_2Zn_{20}$, and provide guidance for optimizing its thermoelectric properties.

II. EXPERIMENTAL METHODS

Single-crystal specimens were synthesized by the molten metal flux technique using the growth protocols described by Torikachvili *et al.* [14] and Jia *et al.* [25,26]. Elements with purities >99.9% were loaded into 2-mL Canfield alumina crucibles [27] with the molar ratio of 1(Ce, Yb) : 2(Ir) : 60(Zn) and 1(Ce, Sm, Yb) : 2(Ir) : 60(Zn). The crucibles were sealed under vacuum in 2-mm-thick quartz tubes (18 mm outer diameter and 14 mm inner diameter), heated to 1050 °C at a rate of 50 °C/h, and held at that temperature for 72 h. The quartz tubes were then cooled down to 700 °C at a rate of 2 °C/h, and held at that temperature for another 72 h. At 700 °C, the excess flux was removed by centrifuging, after which crystals with dimensions of several millimeters were collected.

Elemental analysis was done using an FEI NOVA 400 nanoSEM scanning electron microscope (SEM) with electron-dispersive spectroscopy (EDS) capabilities using an Oxford UltimMAX SDD (silicon drift detector). The structure and unit cell parameters of the single crystals were characterized by single-crystal x-ray diffraction (XRD) using an Oxford-Diffraction Xcalibur2 CCD system with graphite monochromated Mo $K\alpha$ radiation. High-energy XRD data were collected using synchrotron x rays with an energy of 110 keV ($\lambda = 0.1126$ Å). Scattered intensities were collected with a point detector (Ge solid state detector) coupled with a multi-channel analyzer to remove unwanted background scattering. Scattered intensities were collected to Q values of 30 Å^{-1} to achieve high resolution in real space, where the wave vector Q is defined as $Q = 4\pi \sin(\theta)\lambda$ and θ is the Bragg angle. The intensities were converted into atomic pair distribution functions (PDFs) which have proven useful in structure studies on complex materials exhibiting local structural distortions.

Temperature-dependent magnetic susceptibility $\chi(T)$ and isothermal magnetization $M(H)$ measurements were done for single crystals using a Quantum Design vibrating sample magnetometer (VSM) magnetic property measurement system (MPMS). $M(H)$ measurements were performed at a constant temperature $T = 1.8$ K under applied magnetic fields H from −7 to 7 T. $\chi(T)$ measurements were done under a constant magnetic field $H = 0.1$ T for a range of temperatures from 1.8 to 300 K. For both cases, single crystals were mounted such that the magnetic fields were parallel to the (111) planes. Heat capacity (C_p) was measured from 1.8 to 250 K using a Quantum Design physical property measurement system (PPMS). The temperature-dependent Seebeck coefficient S, thermal conductivity κ, and electrical resistivity ρ were measured using the PPMS thermal transport option (TTO). For these measurements, single crystals were cut into rectangular bars with a general dimension of 7 mm × 2 mm × 1 mm. All surfaces were polished in order to reduce surface scattering. TTO measurements were performed from 3 to 400 K, obtaining ρ, κ, and S simultaneously as a function of T in order to assess both ZT and the power factor $PF = S^2\sigma$. Both C_p and TTO measurements were performed under high vacuum ($\approx 10^{-4}$ Torr) with no magnetic field being applied to the specimens.

III. RESULTS AND DISCUSSION

A. Electrical transport and thermoelectric properties

Figure 1(a) shows the temperature-dependent electrical resistivities $\rho(T)$ of all specimens of $Yb_xCe_ySm_zIr_2Zn_{20}$ ($x +$
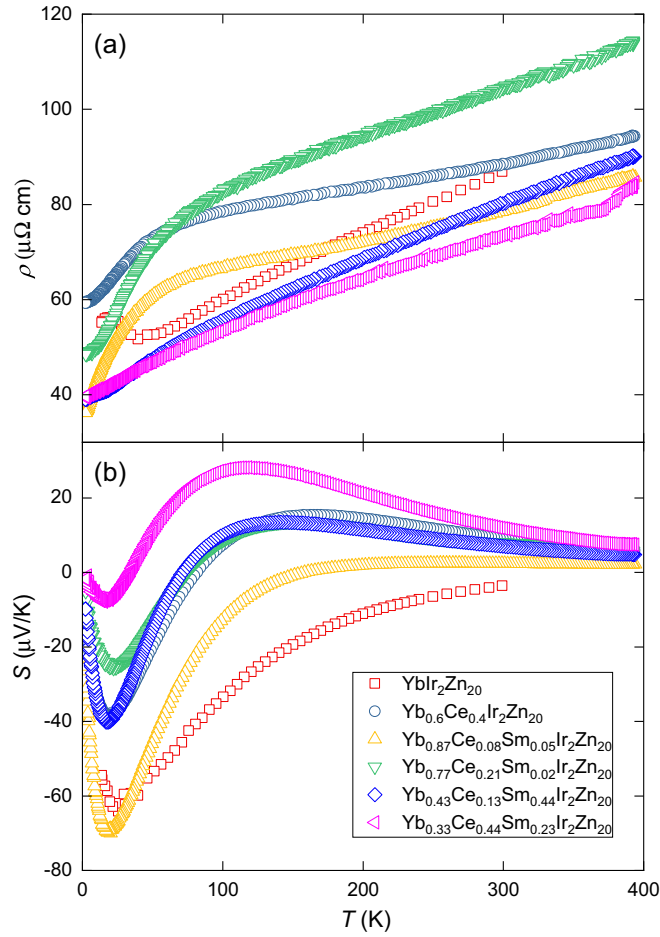
FIG. 1. Temperature-dependent (a) electrical resistivity $\rho(T)$, and (b) Seebeck coefficient $S(T)$ for $Yb_xCe_ySm_zIr_2Zn_{20}$ ($x + y + z = 1$).

FIG. 2. (a) Total thermal conductivity κ vs T, and (b) lattice thermal conductivity κ_L vs T for $Yb_xCe_ySm_zIr_2Zn_{20}$ ($x + y + z = 1$).

$y + z = 1$). Consistent with earlier reports [9,14,20], the parent compound ($YbIr_2Zn_{20}$) exhibits metallic behavior at high temperatures that is followed by a broad minimum near 50 K and a broad maximum near 20 K that are due to hybridization between the f- and conduction electron states [9,14]. The introduction of even small amounts of Ce strongly modifies this behavior, e.g., $\rho(T)$ for $Yb_{0.87}Ce_{0.08}Sm_{0.05}Ir_2Zn_{20}$ develops a shoulder that is centered around 50 K, which is typical for Kondo lattice systems [28]. This behavior persists for the other specimens where Ce is the main substituent, including for $Yb_{0.6}Ce_{0.4}Ir_2Zn_{20}$, and resembles what is seen for $CeIr_2Zn_{20}$ [23]. On the other hand, the presence of large amounts of Sm (e.g., $Yb_{0.43}Ce_{0.13}Sm_{0.44}Ir_2Zn_{20}$ and $Yb_{0.33}Ce_{0.44}Sm_{0.23}Ir_2Zn_{20}$) suppresses the Kondo lattice behavior and strongly drives the system to a more typical metallic behavior [28]. Taken together, these data indicate that increased Ce content tunes the Kondo hybridization temperature towards higher values than those seen for the pure Yb compound, while Sm substitution tends to weaken the hybridization.

The temperature-dependent thermopower $S(T)$ is presented in Fig. 1(b). Similar to earlier reports [8,9], $S(T)$ for the parent compound decreases with decreasing T and reaches a value of -64 µV/K at $T \approx 20$ K. This was earlier
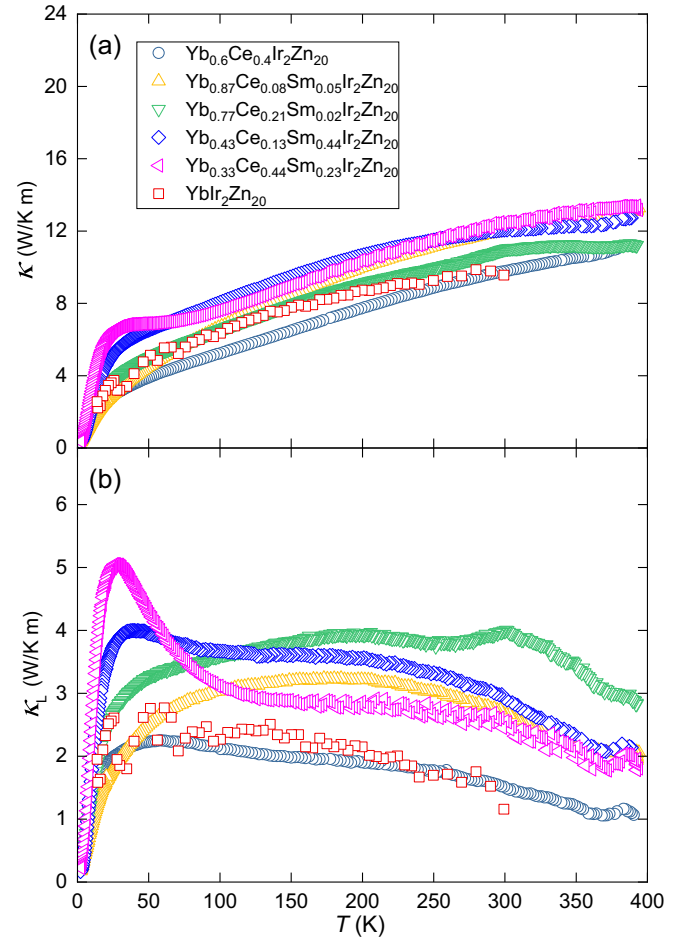
interpreted as being due to Kondo lattice hybridization, where the negative value shows that the charge carriers are mainly electronlike. By introducing 8% Ce and 5% Sm on the Yb site, the peak value is enhanced to -70 µV/K. A further increase of Ce content reduces the magnitude of the negative peak and produces a positive peak at $T \approx 100$ K, which is as a result of Ce-dominated hybridization [29] and resembles what is seen for $CeIr_2Zn_{20}$ [23]. Here, the evolution from positive to negative values demonstrates that while Yb favors an electronlike Fermi surface, Ce produces a holelike Fermi surface. Additional Sm substitution preserves the overall shape of the Ce-substituted samples, but results in further fine tuning of S. Taken together, these results indicate that the mixing of Yb and Ce results in distinct hybridization for the separate sets of f electrons, as well as competition between the electronlike and holelike Fermi surfaces.

The total thermal conductivity $\kappa(T)$ for all the specimens is presented in Fig. 2(a), which is a combination of a lattice term κ_L and an electronic term κ_E. For κ_L, a correction for radiation loss effects has been made following the procedure described in Pope *et al.* [30]. Figure 2(b) shows $\kappa_L(T)$ after the correction. κ_E was obtained through the Wiedemann-Franz relation [31]

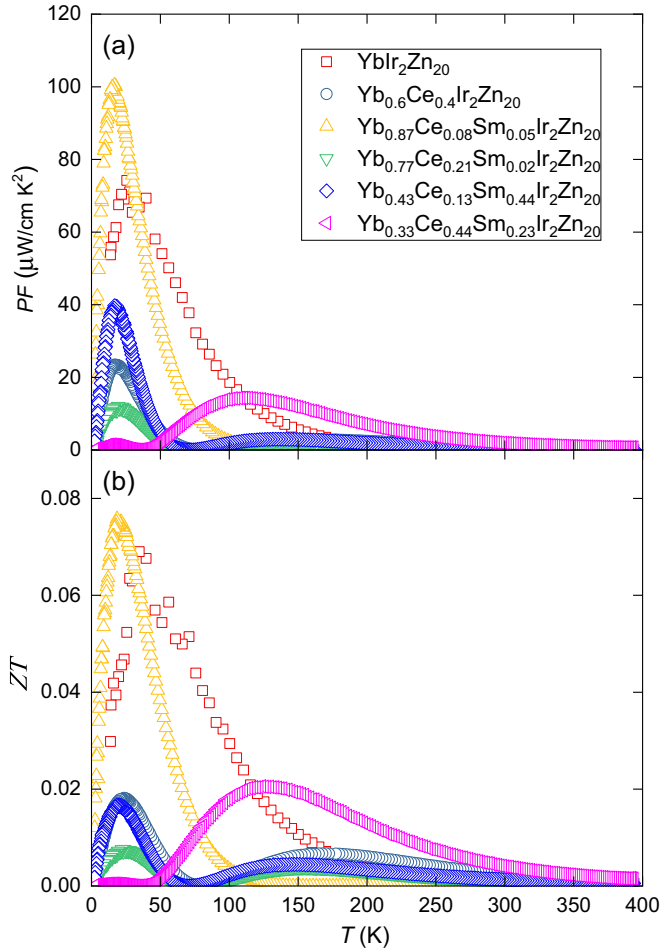$$\kappa_E(T) = \frac{L_0 T}{\rho(T)}, \quad L_0 = 2.44 \times 10^{-8} \text{ W}\,\Omega/\text{K}^2, \quad (1)$$

FIG. 3. Temperature-dependent (a) power factor *PF* and (b) dimensionless figure of merit *ZT* of $Yb_xCe_ySm_zIr_2Zn_{20}$ ($x + y + z = 1$).
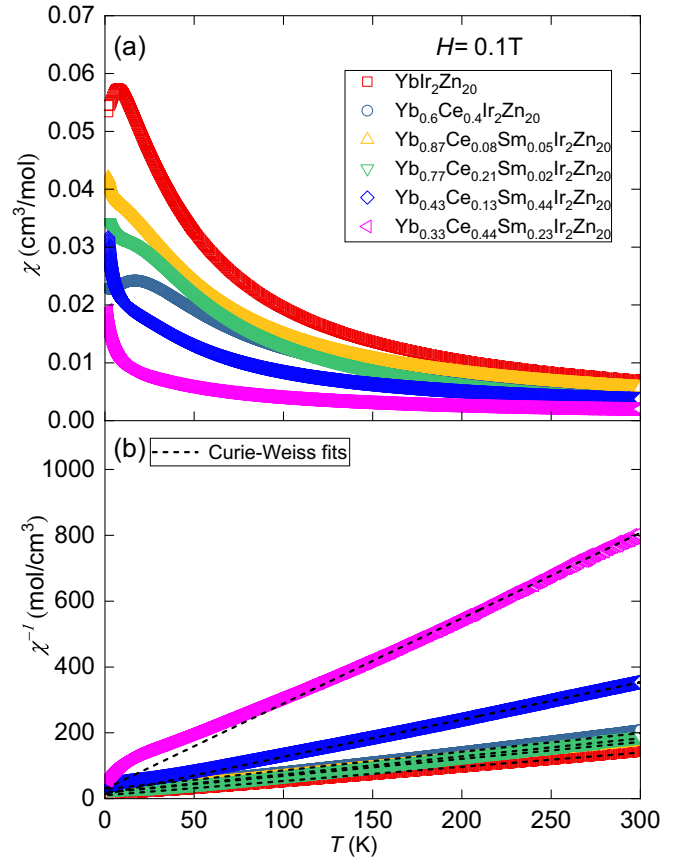

FIG. 4. Temperature-dependent (a) magnetic susceptibility $\chi(T)$ with an applied magnetic field $H = 0.1$ T, and (b) inverse of the magnetic susceptibility $\chi^{-1}(T)$ for $Yb_xCe_ySm_zIr_2Zn_{20}$ ($x + y + z = 1$). The dashed lines represent the Curie-Weiss fits mentioned in the text.

where L_0 represents the Lorentz number. These results will be discussed in detail in Sec. III C, but are presented here in order to calculate the thermoelectric figure of merit *ZT*.

Figure 3 shows the power factors, $PF = S^2/\rho$, and the thermoelectric figures of merit, $ZT = S^2T/(\rho\kappa)$, where S is the Seebeck coefficient, ρ is the electrical resistivity, and κ is the thermal conductivity. The specimen that presents the highest *PF* is $Yb_{0.87}Ce_{0.08}Sm_{0.05}Ir_2Zn_{20}$, with a peak value of 100.55 μW/(cm K^2) at 16.8 K. This value represents an improvement of approximately 35% as compared to the previous reported value for $YbIr_2Zn_{20}$ [9]. This large *PF* and small κ value result in a large *ZT* value for this specimen [Fig. 3(b)], with a peak value of 0.076 at 18.63 K. It can also be observed that for several specimens the *ZT* peaks are shifted to higher temperatures. Between 100 and 200 K, the specimen $Yb_{0.33}Ce_{0.44}Sm_{0.23}Ir_2Zn_{20}$ presented the highest *ZT* peak, with a value of 0.02 at 140.67 K. This specimen also contains triple fillers (Yb, Ce, and Sm) with the highest concentration of Ce among other specimens.

B. Magnetic and heat capacity properties

To better understand the effect of introducing Ce and Sm on the Yb site, the temperature-dependent magnetization was measured, which provides insights into the *f*-electron valence states and the hybridization strength [32–34]. Figure 4(a) presents the temperature-dependent magnetic susceptibility $\chi(T)$ for all specimens, where paramagnetic behavior is observed at elevated temperatures in all cases. Curie-Weiss fits were performed at high temperatures ($T > 150$ K) to the inverse of the magnetic susceptibility [Fig. 4(b)] using the expression [35]

$$\chi(T) + \chi_0(T) = \frac{c}{T - \theta_W}, \qquad (2)$$

where c is the Curie constant (calculated as a fitting parameter), and θ_W is the Weiss temperature. In some cases, an additional χ_0 term was needed to fit the data, which may be due to a Van Vleck contribution that originates from the Sm ions [36]. Table I shows θ_W for all the specimens, together with the experimental effective magnetic moment $\mu_{eff} = 2.82\sqrt{c/n}$, where n represents the number of magnetic elements per formula unit [31]. These values are compared to the theoretical effective magnetic moment for trivalent ions [35], $\mu_{eff,Th} = x \cdot \mu_{eff(Ce)} + y \cdot \mu_{eff(Sm)} + z \cdot \mu_{eff(Yb)}$, where $x + y + z = 1$. The parent compound, $YbIr_2Zn_{20}$, has also been included for comparison. By comparing the theoretical and experimental total effective magnetic moments of all the specimens (Table I), it is seen that the values are in good
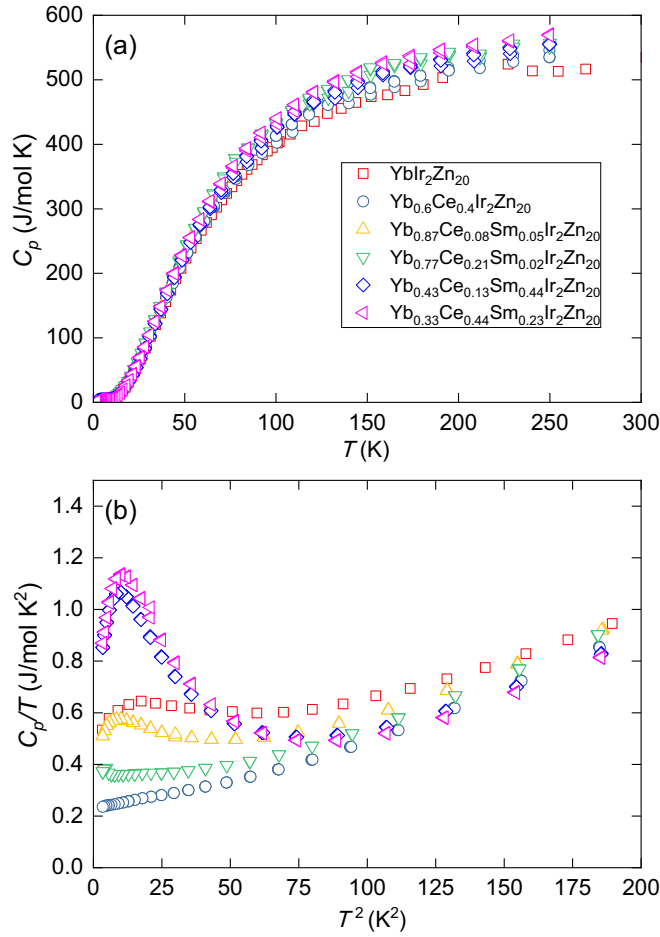
FIG. 5. (a) C_p vs T and (b) C_p/T vs T^2 for $Yb_xCe_ySm_zIr_2Zn_{20}$ $(x + y + z = 1)$.

agreement, which indicates that the ions remain trivalent for all substitutions.

Heat capacity measurements (Fig. 5) provide further insights about the evolution of the electronic hybridization and the lattice behavior. Starting with the parent compound ($YbIr_2Zn_{20}$), it is seen that there is a Fermi-liquid dependence [37] $C_p/T = \gamma + \beta T^2$ for 10 K $< T <$ 14 K, where γ and β represent the electronic and lattice contributions to the heat capacity. But this dependence is interrupted by a broad hump at low temperatures [Fig. 5(b)], which indicates the presence of additional electronic degrees of freedom at low temperatures. Despite this, it can be seen that over this temperature range chemical substitution has only a weak effect on the electronic contribution to the heat capacity. However, a stronger evolution is seen at lower temperatures. Focusing first on the samples that primarily substitute Ce, it can be observed that the low-temperature value is suppressed with increasing Ce content, which is consistent with earlier results showing that for $CeIr_2Zn_{20}$ there is simple Fermi-liquid behavior with $\gamma = 87$ mJ mol^{-1} K^{-2} [23]. The Sm case is potentially more complex given that $SmIr_2Zn_{20}$ exhibits a low-temperature hump that originates from magnetic fluctuations of the Sm ions that eventually resolves into an ordered magnetic state [38]. The temperatures at which all these broad humps appear agree with the magnetic ordering observed in $\chi(T)$ [Fig. 4(a)].
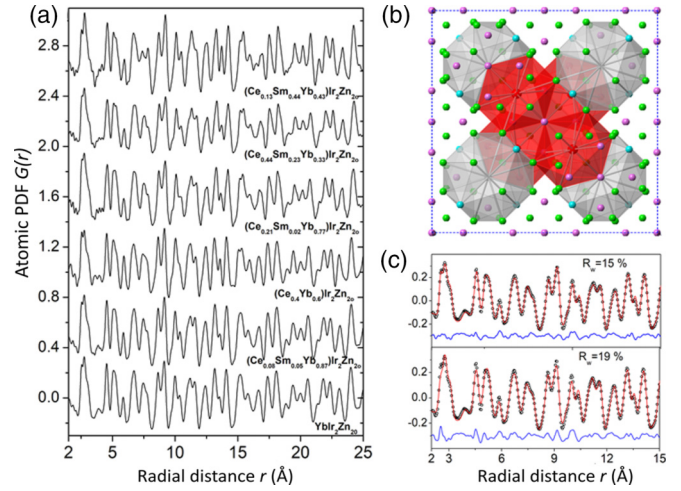

FIG. 6. (a) Experimental atomic PDFs reflecting the atomic arrangement in the respective system. The data of each sample is offset for a clear presentation. (b) Polyhedron representation of the unit cell, where R is represented in black, Ir in red, Zn_1, Zn_2, and Zn_3 in green, magenta, and blue respectively. (c) Fit (red line) to the experimental (symbols) atomic PDF for $YbIr_2Zn_{20}$. In the fit on top, anisotropic thermal factors are refined. In the bottom fit, the thermal factors are kept isotropic. The residual difference (blue line) is shifted by a constant factor for clarity. The goodness-of-fit indicators R_w are given.

Therefore, we suspect these humps are associated with the magnetic contribution due to the Yb, Ce, and Sm ions. However, we cannot rule out the possibility that the Schottky anomaly also contributes to this behavior, as described by Torikachvili *et al.* [14]. As a result, it is very challenging to extract an accurate γ from a low-temperature fit, so only β is being reported for all samples (Table I). To better understand the lattice dynamic, the full temperature range of the heat capacity has been fitted using the combined Debye-Einstein model, where $C_p(T)$ can be expressed as [39]

$$C_p = C_D\left(\frac{T}{\theta_D}\right)^3 \int_0^{\theta_D/T} \frac{x^4 e^x}{(e^x - 1)^2}dx + C_E\left(\frac{\theta_E}{T}\right)^2 \frac{e^{\theta_E/T}}{\left(e^{\theta_E/T} - 1\right)^2}, \tag{3}$$

where $x = \hbar\omega/\kappa_B T$, ω is the Debye frequency, θ_D and θ_E are the Debye and Einstein temperatures, respectively, and C_D and C_E are constants containing numbers of oscillators and degrees of freedom. All calculated parameters are listed in Table I, where θ_D and θ_E vary little for different concentrations.

C. High-energy XRD and atomic pair distribution function (PDF) analysis

The atomic structure was studied by high-energy XRD coupled to an atomic pair distribution function (PDF) analysis. The technique has proven useful in studying materials exhibiting lattice distortions, including thermoelectric materials [40–42]. Experimental atomic PDFs are shown in Fig. 6(a). The PDFs show a sequence of well-defined peaks. The area under a peak is proportional to the number of atomic pairs
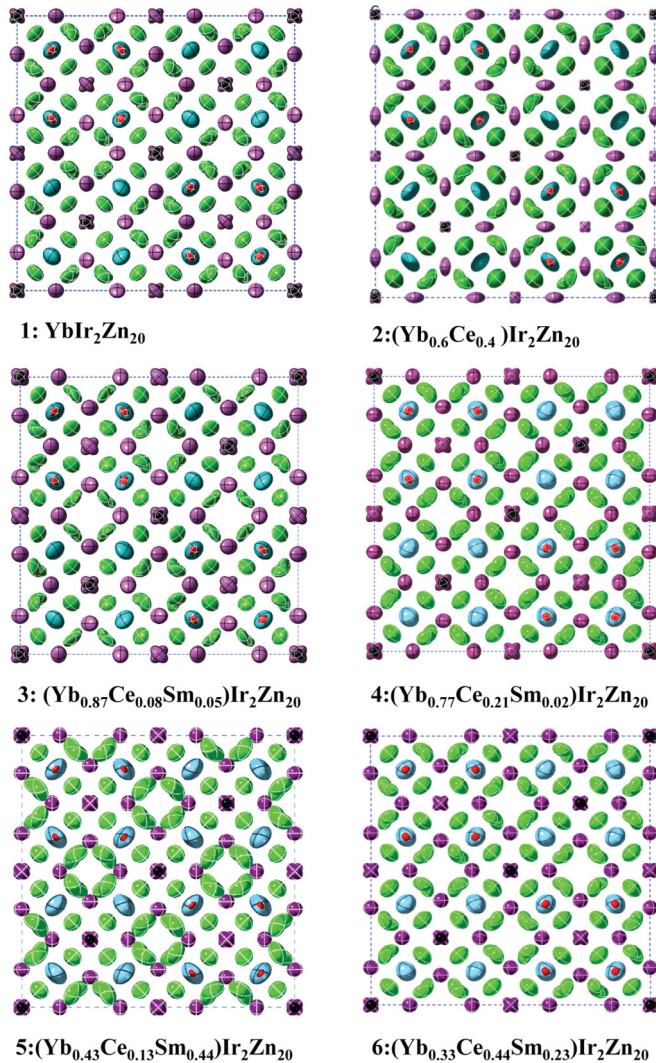
FIG. 7. Projection of the refined unit cells of $Yb_xCe_ySm_zIr_2Zn_{20}$ $(x + y + z = 1)$, where R is represented in black, Ir in red, and Zn_1, Zn_2, and Zn_3 in green, magenta, and blue, respectively. Mean-square displacements for Zn atoms are much larger and anisotropic than those for metal atoms.
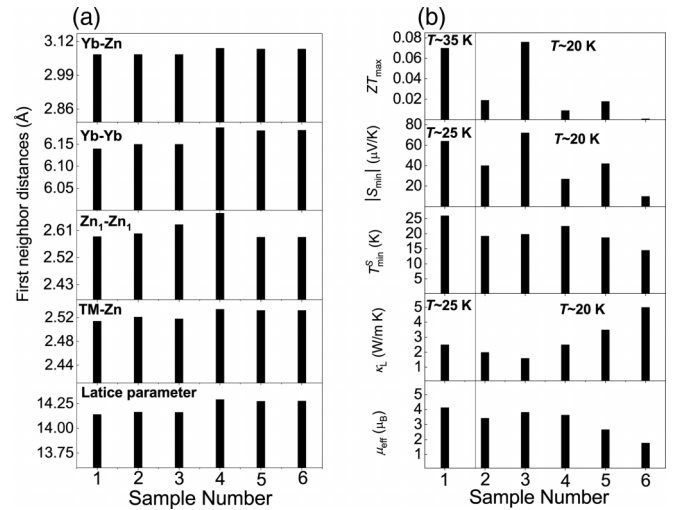

FIG. 8. (a) Lattice parameters and selected interatomic distances derived from the PDF refined models, and (b) selected property data. Specimen compositions are listed in Table I.

separated by the particular interatomic vector [41]. In particular, the first PDF peak reflects the first coordination sphere in studied materials. It splits into three compounds reflecting distinct Zn-Zn, R-Zn, and T-Zn bonding distances, where R and T are rare-earth and transition metal elements, respectively. In the compounds, R atoms have 16 Zn neighbors forming a Frank-Kasper polyhedron and T atoms have 12 first neighbors, as shown in Fig. 6(b). On the other hand, Zn atoms occupy three distinct positions, Zn_1 (Wyckoff position $96g$), Zn_2 (Wyckoff position $48f$), and Zn_3 (Wyckoff position $16c$), where Zn_1 and Zn_2 atoms are 12-fold coordinated and Zn_3 atom is 14-fold coordinated. Hence, Zn_3 may be expected to exhibit large atomic displacements, where the displacements of Zn_1 and Zn_2 would be smaller. In addition, because Zn_1 has both Ir and lanthanides as first neighbors, its displacements from the average position may be expected to vary with changes in the lanthanide type. The atomic PDFs were fit with a structural model based on the well-known crystal

structure of RT_2Zn_{20} compounds [18]. The fit parameters included lattice parameters (Table I), coordinates of Zn_1 and Zn_2 atoms, and mean-squared atomic displacements (MSD). A model based on isotropic displacements, however, did not fit well the first PDF peak as shown in Fig. 6(c). A model based on anisotropic displacements performs much better (R_w of 15% vs 19%).

Projections of the refined unit cells are shown in Fig. 7. It can be observed that Zn atoms suffer large anisotropic displacements, where the preferred direction of the displacements and their magnitude are different for different compounds. The observed anharmonicity of the atomic vibrations of Zn atoms would lead to a diminished κ_L. The decrease would be different for different compounds, as illustrated in Fig. 2. Note, as the small atomic displacements indicate, the contribution of R and Ir atoms to the observed diminishing of κ would be limited.

Refined lattice parameters and selected interatomic distances derived from the PDF refined models are shown in Fig. 8(a). It is seen that a partial replacement of Yb atoms by Ce atoms expands the lattice parameter, Yb-Yb distances, and coordination polyhedra of Yb and Ir atoms. This is because Ce atoms are larger in size than Yb atoms. Distances between nearby Zn atoms do not scale with Ce content, indicating a uniform distortion of the Zn framework upon introducing Ce. Split positions for Zn atoms were considered but proved to be nonrealistic. Increased MSD did a better job, indicating that the Zn sublattice/framework is continuous and just distorted/softened. The observed expansion of unit cell volume and coordination polyhedra of R and Ir atoms, i.e., negative pressure, would affect significantly the electronic properties of the studied compounds. In particular, negative pressure and a coupled increase of the volume of the Yb cage would reduce partially the valence state of magnetic Yb^{3+} ions toward the nonmagnetic Yb^{2+} state, resulting in diminished μ_{eff} as documented by our measurements (see Table I). The enhanced degree of hybridization would increase the density of states at the Fermi level when compared to the limiting

Yb^{3+} and Yb^{2+} states. This may explain the emergence of a "negative" dip in $S(T)$ at low temperatures [Fig. 1(b)]. The combined effect of increased (negative) Seebeck coefficient and diminished lattice conductivity would result in increased PF and ZT, as observed in Fig. 3.

Selected property data are also shown in Fig. 8(b). Inspection of the data indicates a strong correlation between the thermoelectric (ZT, κ_L, and S) and structural properties (lattice parameters and near-neighbor distances) of 100% Yb and 87% Yb samples.

IV. CONCLUSIONS

We have investigated the effects on the magnetic, thermal, and thermoelectric properties of 1-2-20 compounds when introducing other rare-earth elements (Ce and Sm) in the compound that motivated this study (YbIr$_2$Zn$_{20}$). The electrical resistivity data suggest that by introducing Ce and Sm, a variation in the Kondo coherence temperature can be observed. Heat capacity data show that chemical substitution has only a weak effect on both the electronic contribution to the heat capacity and the average lattice behavior. XRD data show

strong lattice anharmonicity (the Zn sublattice is "soft," i.e., phonon glass, as indicated by the observed large MSD), which typically reduces the lattice thermal conductivity. Overall, our results indicate that it is possible to improve the thermoelectric properties of 1-2-20 compounds by introducing multiple rare-earth elements as cage fillers. The specimen that has the largest ZT is $Yb_{0.87}Ce_{0.08}Sm_{0.05}Ir_2Zn_{20}$ with an absolute value of the Seebeck coefficient of 70 μV/K and a ZT of 0.076, at 20 K. Finally, having ZT peaks at higher temperatures (100–200 K) for the Ce-content specimens is also an interesting result. It opens up opportunities for applications under broader temperatures.

[1] I. Dincer, *Refrigeration Systems and Applications*, 3rd ed. (Wiley, Hoboken, NJ, 2017).

[2] G. S. Nolas, J. Sharp, and J. Goldsmid, *Thermoelectrics: Basic Principles and New Materials Developments*, Vol. 45 (Springer, Berlin, 2001).

[3] G. Mahan and J. Sofo, The best thermoelectric, Proc. Natl. Acad. Sci. USA **93**, 7436 (1996).

[4] G. A. Slack, New materials and performance limits for thermoelectric cooling, in *CRC Handbook of Thermoelectrics*, edited by D. M. Rowe (CRC Press, Boca Raton, FL, 1995), 1st ed., Chap. 34, pp. 407–440.

[5] B. C. Sales, Novel thermoelectric materials, Curr. Opin. Solid State Mater. Sci. **2**, 284 (1997).

[6] D. T. Morelli, Thermoelectric materials, in *Springer Handbook of Electronic and Photonic Materials*, edited by S. Kasap and P. Capper (Springer, Berlin, 2017), pp. 1–1.

[7] T. Tritt, Thermoelectric materials: principles, structure, properties, and applications, in *Encyclopedia of Materials: Science and Technology* (Elsevier, Amsterdam, 2002), pp. 1–11.

[8] E. Mun, S. Jia, S. L. Bud'ko, and P. C. Canfield, Thermoelectric power of the YbT$_2$Zn$_{20}$ (T = Fe, Ru, Os, Ir, Rh, and Co) heavy fermions, Phys. Rev. B **86**, 115110 (2012).

[9] K. Wei, J. N. Neu, Y. Lai, K.-W. Chen, D. Hobbis, G. S. Nolas, D. E. Graf, T. Siegrist, and R. E. Baumbach, Enhanced thermoelectric performance of heavy-fermion compounds YbTM_2Zn$_{20}$ (TM = Co, Rh, Ir) at low temperatures, Sci. Adv. **5**, eaaw6183 (2019).

[10] M. Beekman, D. T. Morelli, and G. S. Nolas, Better thermoelectrics through glass-like crystals, Nat. Mater. **14**, 1182 (2015).

[11] M. Tsujimoto, Y. Matsumoto, T. Tomita, A. Sakai, and S. Nakatsuji, Heavy-Fermion Superconductivity in the Quadrupole Ordered State of PrV$_2$Al$_{20}$, Phys. Rev. Lett. **113**, 267001 (2014).

[12] C. Bhandari, Thermoelectric transport theory, in *CRC Handbook of Thermoelectrics*, (Ref. [4]), Chap. 4, pp. 27–40.

[13] G. Nolas, D. Morelli, and T. M. Tritt, Skutterudites: A phonon-glass-electron crystal approach to advanced thermoelectric energy conversion applications, Annu. Rev. Mater. Sci. **29**, 89 (1999).

[14] M. Torikachvili, S. Jia, E. Mun, S. Hannahs, R. Black, W. Neils, D. Martien, S. Bud'Ko, and P. Canfield, Six closely related YbT$_2$Zn$_{20}$ (T = Fe, Co, Ru, Rh, Os, Ir) heavy fermion compounds with large local moment degeneracy, Proc. Natl. Acad. Sci. USA **104**, 9960 (2007).

[15] A. L. Cornelius, J. M. Lawrence, T. Ebihara, P. S. Riseborough, C. H. Booth, M. F. Hundley, P. G. Pagliuso, J. L. Sarrao, J. D. Thompson, M. H. Jung, A. H. Lacerda, and G. H. Kwei, Two Energy Scales and Slow Crossover in YbAl$_3$, Phys. Rev. Lett. **88**, 117201 (2002).

[16] Y. Hirose, M. Toda, S. Yoshiuchi, S. Yasui, K. Sugiyama, F. Honda, M. Hagiwara, K. Kindo, R. Settai, and Y. Ōnuki, Metamagnetic transition in heavy fermion compounds YbT$_2$Zn$_{20}$ (T: Co, Rh, Ir), J. Phys.: Conf. Ser. **273**, 012003 (2011).

[17] G. Nolas, M. Kaeser, R. Littleton IV, and T. Tritt, High figure of merit in partially filled ytterbium skutterudite materials, Appl. Phys. Lett. **77**, 1855 (2000).

[18] T. Nasch, W. Jeitschko, and U. C. Rodewald, Ternary rare earth transition metal zinc compounds RT_2Zn$_{20}$ with T = Fe, Ru, Co, Rh, and Ni, Z. Naturforsch. B **52**, 1023 (1997).

[19] S. Yoshiuchi, M. Toda, M. Matsushita, S. Yasui, Y. Hirose, M. Ohya, K. Katayama, F. Honda, K. Sugiyama, M. Hagiwara *et al.*, Heavy fermion state in YbIr$_2$Zn$_{20}$, J. Phys. Soc. Jpn. **78**, 123711 (2009).

[20] T. Takeuchi, S. Yasui, M. Toda, M. Matsushita, S. Yoshiuchi, M. Ohya, K. Katayama, Y. Hirose, N. Yoshitani, F. Honda *et al.*, Metamagnetic behavior in heavy-fermion compound YbIr$_2$Zn$_{20}$, J. Phys. Soc. Jpn. **79**, 064609 (2010).

[21] B. Lenoir, M. Cassart, J.-P. Michenaud, H. Scherrer, and S. Scherrer, Transport properties of Bi-rich Bi-Sb alloys, J. Phys. Chem. Solids **57**, 89 (1996).

[22] A. Doroshenko, E. Rogacheva, A. Drozdova, K. Martynova, and Y. V. Men'shov, Thermoelectric properties of polycrystalline $Bi_{1-x}Sb_x$ solid solutions in the concentration range $x = 0$–0.25, J. Thermoelectr. **4**, 23 (2016).

[23] P. Swatek and D. Kaczorowski, Intermediate valence behavior in the novel cage compound $CeIr_2Zn_{20}$, J. Phys.: Condens. Matter **25**, 055602 (2013).

[24] Y. Isikawa, T. Mizushima, A. Fujita, and T. Kuwai, Magnetic and thermal properties of $SmRh_2Zn_{20}$ single crystal, J. Phys. Soc. Jpn. **85**, 024707 (2016).

[25] S. Jia, N. Ni, S. Bud'ko, and P. Canfield, Magnetic properties of $Gd_xY_{1-x}Fe_2Zn_{20}$: Dilute, large-S moments in a nearly ferromagnetic Fermi liquid, Phys. Rev. B **76**, 184410 (2007).

[26] S. Jia, S. Bud'ko, G. Samolyuk, and P. Canfield, Nearly ferromagnetic Fermi-liquid behaviour in YFe_2Zn_{20} and high-temperature ferromagnetism of $GdFe_2Zn_{20}$, Nat. Phys. **3**, 334 (2007).

[27] P. C. Canfield, T. Kong, U. S. Kaluarachchi, and N. H. Jo, Use of frit-disc crucibles for routine and exploratory solution growth of single crystalline samples, Philos. Mag. **96**, 84 (2016).

[28] P. Coleman, Heavy fermions: Electrons at the edge of magnetism, in *Handbook of Magnetism and Advanced Magnetic Materials*. edited by H. Kronmuller and S. Parkin (Wiley, Hoboken, NJ, 2007), Vol. I, pp. 95–148.

[29] A. Fujimori and J. Weaver, $4f$-$5d$ hybridization and the α-γ phase transition in cerium, Phys. Rev. B **32**, 3422 (1985).

[30] A. Pope, B. Zawilski, and T. Tritt, Description of removable sample mount apparatus for rapid thermal conductivity measurements, Cryogenics **41**, 725 (2001).

[31] C. Kittel, *Introduction to Solid State Physics*, 8th ed. (Wiley, Hoboken, NJ, 2021).

[32] W. Zhao, P. Wei, Q. Zhang, C. Dong, L. Liu, and X. Tang, Enhanced thermoelectric performance in barium and indium double-filled skutterudite bulk materials via orbital hybridization induced by indium filler, J. Am. Chem. Soc. **131**, 3713 (2009).

[33] Z.-H. Zheng, P. Fan, J.-T. Luo, and G.-X. Liang, Hybridization of electronic band structure and enhancement of thermoelectric properties of ZnSb thin film by In doping, J. Phys. Chem. Solids **103**, 82 (2017).

[34] D. Zhang, J. Yang, H. Bai, Y. Luo, B. Wang, S. Hou, Z. Li, and S. Wang, Significant average *ZT* enhancement in Cu_3SbSe_4-based thermoelectric material via softening $p-d$ hybridization, J. Mater. Chem. A **7**, 17648 (2019).

[35] S. Blundell, *Magnetism in Condensed Matter* (Oxford University Press, Oxford, UK, 2007).

[36] M. Janoschek, R. E. Baumbach, J. J. Hamlin, I. K. Lum, and M. B. Maple, The non-centrosymmetric heavy fermion ferromagnet $Sm_2Fe_{12}P_7$, J. Phys.: Condens. Matter **23**, 094221 (2011).

[37] S. Stefanoski, J. Martin, and G. Nolas, Low temperature transport properties and heat capacity of single-crystal Na_8Si_{46}, J. Phys.: Condens. Matter **22**, 485404 (2010).

[38] Y. Taga, K. Sugiyama, K. Enoki, Y. Hirose, K. Iwakawa, A. Mori, K. Ishida, T. Takeuchi, M. Hagiwara, K. Kindo *et al.*, Magnetic properties of RIr_2Zn_{20} (*R*: rare earth) with the caged structure, J. Phys. Soc. Jpn. **81**, SB051 (2012).

[39] T. Besara, D. Ramirez, J. Sun, J. Whalen, T. Tokumoto, S. McGill, D. Singh, and T. Siegrist, Ba_2TeO: A new layered oxytelluride, J. Solid State Chem. **222**, 60 (2015).

[40] V. Petkov, Nanostructure by high-energy x-ray diffraction, Mater. Today **11**, 28 (2008).

[41] V. Petkov, Pair distribution functions analysis, *Characterization of Materials* (Wiley, Hoboken, NJ, 2012), pp. 1361–1372.

[42] H. Lin, E. Božin, S. Billinge, J. Androulakis, C. Malliakas, C. Lin, and M. Kanatzidis, Phase separation and nanostructuring in the thermoelectric material $PbTe_{1-x}S_x$ studied using the atomic pair distribution function technique, Phys. Rev. B **80**, 045204 (2009).